Polarization Boost and Ferroelectricity Down to One Unit Cell in Layered Carpy-Galy La2Ti2O7 Thin Films

Elzbieta Gradauskaite, Anouk Goossens, Xiaoyan Li, Lucía Iglesias, Alexandre Gloter, Quintin Meier, Manuel Bibes

▶ **To cite this version:**

Elzbieta Gradauskaite, Anouk Goossens, Xiaoyan Li, Lucía Iglesias, Alexandre Gloter, et al.. Polarization Boost and Ferroelectricity Down to One Unit Cell in Layered Carpy-Galy La2Ti2O7 Thin Films. Advanced Materials, 2025, 37 (12), pp.2416963. ⟨10.1002/adma.202416963⟩. ⟨hal-05384419⟩

HAL Id: hal-05384419

https://hal.science/hal-05384419v1

Submitted on 27 Nov 2025

HAL is a multi-disciplinary open access archive for the deposit and dissemination of scientific research documents, whether they are published or not. The documents may come from teaching and research institutions in France or abroad, or from public or private research centers.

L'archive ouverte pluridisciplinaire **HAL**, est destinée au dépôt et à la diffusion de documents scientifiques de niveau recherche, publiés ou non, émanant des établissements d'enseignement et de recherche français ou étrangers, des laboratoires publics ou privés.

HAL Authorization

Polarization Boost and Ferroelectricity Down to One Unit Cell in Layered Carpy-Galy $La_2Ti_2O_7$ Thin Films

Elzbieta Gradauskaite, Anouk S. Goossens, Xiaoyan Li, Lucía Iglesias, Alexandre Gloter, Quintin N. Meier, and Manuel Bibes*

Layered perovskite-based compounds offer a range of unconventional properties enabled by their naturally anisotropic structure. Among these, the Carpy-Galy phases ($A_nB_nO_{3n+2}$), characterized by (110)-oriented perovskite planes interleaved with additional oxygen layers, stand out for robust in-plane polarization. However, the challenges associated with the synthesis of ultrathin Carpy-Galy films and understanding the impact of strain on their properties limit their integration into devices. Here, $La_2Ti_2O_7$ ($n = 4$) films grown on substrates imposing tensile, compressive, or negligible epitaxial strains are investigated. Surprisingly, a 3% tensile strain from $DyScO_3$ (100) substrates facilitates layer-by-layer growth mode, whereas compressive ($LaAlO_3$-Sr_2TaAlO_6 (110)) or negligible ($SrTiO_3$ (110)) epitaxial strains require post-deposition annealing to reach comparable crystallinity. Using density-functional theory calculations, scanning probe microscopy, X-ray diffraction, scanning transmission electron microscopy, and polarization switching experiments, it is confirmed that these films possess exceptional ferroelectric properties, including a polarization of 18 μCcm^{-2} – more than three times higher than previously reported – as well as persistence of ferroelectricity down to a single-unit-cell thickness. This study not only advances the understanding of Carpy-Galy phases as epitaxial thin films but also lays a foundation for their integration into advanced ferroelectric device architectures.

1. Introduction

To date, extensive research on low-energy, non-volatile ferroelectric memory has predominantly focused on classical perovskite oxides. The polar behavior in these materials arises from the displacement of cations with respect to anions, leading to an off-centering of positive charges within their oxygen octahedral cages. The straightforward and nearly cubic structure of perovskite oxides simplifies their fabrication into epitaxial thin films, facilitating their integration into complex epitaxial heterostructures. However, perovskite oxides are prone to finite-size effects,[1] which restrict their scalability in nanodevice applications. This limitation has driven the search for alternative materials with more durable polar properties that can combine additional functionalities within the same phase. Among non-traditional ferroelectrics, such as improper ferroelectrics,[2,3] HfO_2-based ferroelectric thin films,[4] 2D polar materials,[5] organic-inorganic hybrid ferroelectrics,[6] layered ferroelectrics[7] are distinguished by their high structural flexibility and robust ferroelectric properties.

Layered ferroelectrics[7] consist of periodically repeating perovskite-like slabs interleaved with spacers that carry localized ionic charges, significantly influencing the electrostatic boundary conditions. Ferroelectricity in these structures is primarily stabilized by the confinement effects of their large periodic unit cells rather than by electronic hybridization within the ABO_3 units (A and B represent cations of different sizes and coordination), thereby enhancing their stability and robustness compared to traditional ferroelectric perovskites. Historically, layered ferroelectrics have been challenging to synthesize, limiting their study mostly to bulk crystals or ceramics. Recent advances, however, have facilitated the preparation of these materials in thin-film form through molecular beam epitaxy and pulsed laser deposition (PLD). It has been demonstrated that epitaxial stabilization of layered ferroelectrics can lead to unprecedented functionality, such as lack of critical thickness for ferroelectricity,[8–11] charged domain walls,[9,12,13] polar vortex topologies,[13] and significantly improved robustness against ferroelectric fatigue.[9] Additionally, integrating layered ferroelectrics into canonical perovskite heterostructures has emerged as a novel approach to mitigate depolarizing field effects and enable the formation of unique polar textures characterized by their chirality.[14]

E. Gradauskaite, A. S. Goossens, L. Iglesias, M. Bibes
Laboratoire Albert Fert, CNRS, Thales
Université Paris Saclay
91767 Palaiseau, France
E-mail: elzbieta.gradauskaite@cnrs-thales.fr
X. Li, A. Gloter
Laboratoire de Physique des Solides
CNRS, Université Paris Saclay
91405 Orsay, France
Q. N. Meier
Université Grenoble Alpes, CNRS, Institut Néel
38042 Grenoble, France

The most extensively studied families of layered ferroelectrics as epitaxial films are the Ruddlesden-Popper phases, due to their superconducting properties,[15,16] and the Aurivillius phases, known for their exceptional resistance to ferroelectric fatigue.[17] However, the layered $A_nB_nO_{3n+2}$ ferroelectrics,[18–22] recently termed the Carpy Galy (CG) phases,[23] have been rarely investigated as thin films. Characterized by 110-oriented perovskite planes interleaved with additional oxygen layers, the CG phases exhibit unparalleled ferroelectric Curie temperature (T_c) values of up to 2000 °C – particularly for $n = 4$ ferroelectrics – and substantial polarization. The dominant ferroelectric instability in the CG phases originates from oxygen octahedra rotations that are prevalent in many magnetically ordered non-polar perovskites. The truncation of the unit cell, however, implies that such oxygen octahedra rotations sum up to a non-zero net polarization in the CG unit cell, a phenomenon coined as proper topological ferroelectricity.[24] Additionally, CG compounds have been debated to be potential material platforms for hosting incommensurate phases,[25,26] multiferroicity,[24,27] as well as polar metallicity.[28] Despite their considerable potential, synthesizing high-quality single-crystalline CG thin films poses significant challenges and a thorough understanding of their ferroelectric properties under diverse epitaxial strain states is still lacking, hindering the optimization of these materials for practical applications.

Here we report on the synthesis of uniaxial in-plane-polarized single-crystalline $La_2Ti_2O_7$ (LTO) $n = 4$ thin films of the Carpy-Galy (CG) phase on various substrates that exert negligible, tensile, and compressive epitaxial strains. In-situ monitoring with reflection high-energy electron diffraction (RHEED) allows us to follow the growth dynamics and uncover how epitaxial strain influences the layering of the CG phase in thin films. Remarkably, we observe that while negligible epitaxial strain results in the layer-by-layer coverage of pseudo-perovskite blocks with disordered oxygen planes, applying some epitaxial strain is crucial for stabilizing a true layer-by-layer growth mode, during which full $A_2B_2O_7$ electroneutral units coalesce to form a continuous film. Notably, substantial tensile strain within the film plane facilitates phase-pure, layer-by-layer growth of films up to tens of nanometers thick without the need for post-deposition annealing. This observation is rationalized by the relationship between polar distortion modes and different epitaxial strains through density-functional theory (DFT) calculations. The combination of X-ray diffraction (XRD), scanning transmission electron microscopy (STEM), piezoresponse force microscopy (PFM), and ferroelectric switching experiments allows us to confirm the synthesis of epitaxial single-crystalline LTO films. The importance of epitaxial strain in stabilizing high-quality thin films is exemplified by more than a threefold enhancement in ferroelectric polarization compared to the literature values reported for bulk single crystals. The films exhibit two-variant nanoscale ferroelectric domain patterns characterized by clearly defined uniaxial in-plane polarization. Lastly, we demonstrate the absence of critical thickness for ferroelectricity in the films of the CG phase and reveal the domain formation mechanism related to the out-of-phase boundary formation at the substrate interface. These insights pave the way for controlled synthesis of phase-pure ferroelectric CG thin films, opening avenues for their integration into functional perovskite-based heterostructures.

2. Results and Discussion

2.1. In situ Monitoring of Strain-Driven Layering in Epitaxial LTO Films

For our study, we selected LTO as a representative $n = 4$ ferroelectric[29] of the CG phase, with the empirical formula $A_2B_2O_7$. LTO, likely the most investigated ferroelectric in the CG family, possesses a monoclinic unit cell (space group $P2_1$)[30] and a ferroelectric Curie temperature (T_c) of about 1500 °C.[29] The crystallographic *c*-axis is oriented perpendicular to the oxygen spacers, the *a*-axis aligns along infinite chains of oxygen octahedra, and the *b*-axis extends through the opposite edges of these octahedra[20] (refer to **Figure 1a**). Notably, LTO exhibits a net polarization along the *b*-axis.[23,29] To fabricate thin films with in-plane polarization, we aim to stabilize single-crystalline 001-oriented LTO on three substrates: $SrTiO_3$ (STO) (110), $DyScO_3$ (DSO) (100), and $LaAlO_3$-Sr_2TaAlO_6 (LSAT) (110), which impart negligible, tensile, and compressive epitaxial strain to the LTO unit cell, respectively (see insets of Figure 1b–d). Note S1 (Supporting Information) presents schematics illustrating the epitaxial relationship between the monoclinic unit cell of the film and the cubic or orthorhombic substrates, accompanied by the corresponding strain calculations.

In order to optimize PLD growth conditions of epitaxial LTO thin films we used RHEED in-situ monitoring, which allowed us to track the film roughness and its crystallinity with respect to the deposition time, and to determine whether the growth is 2D or 3D. For STO (110) substrates, which impart minimal strain, achieving high-quality films required high substrate temperature, low oxygen partial pressure, and a low laser repetition rate, consistent with earlier reports.[31–35] Figure 1b displays the time-dependent intensity of the RHEED signal for an LTO film with oscillations confirming a layer-by-layer growth mode, followed by a clear drop in intensity after the first four oscillations (see caption for deposition parameters). Ex situ X-ray reflectometry (XRR) reveals that each RHEED oscillation corresponds to the deposition of approximately one perovskite-like ABO_3 layer. The higher intensity oscillations at the beginning of the growth, with a consistent count of four, point to the initial growth of $LaTiO_3$ layers at the substrate interface (marked in green). Once this thickness is exceeded, in accordance with the stoichiometry of the ceramic target, oxygen planes are introduced and seem to increase the surface roughness, explaining the observed drop in RHEED intensity (orange).

Next, we investigated the impact of epitaxial strain on the film growth. Remarkably, when LTO film deposition was performed under identical conditions but with tensile in-plane strain provided by the DSO (100) substrate, we observed distinctively different growth dynamics, as depicted in Figure 1c. The RHEED oscillations display higher intensity amplitude and significantly lower frequency (marked in blue), with one oscillation corresponding to every four on the STO (110) substrate (cf. Figure 1b). Post-deposition XRR measurements unambiguously relate each RHEED oscillation to a full $A_2B_2O_7$ unit cell of the CG phase, rather than to the pseudo-perovskite ABO_3 units observed during deposition on STO (110). This indicates the formation of islands comprising the entire electroneutral LTO unit cell, each 1.3 nm in height, which subsequently coalesce to create atomically flat

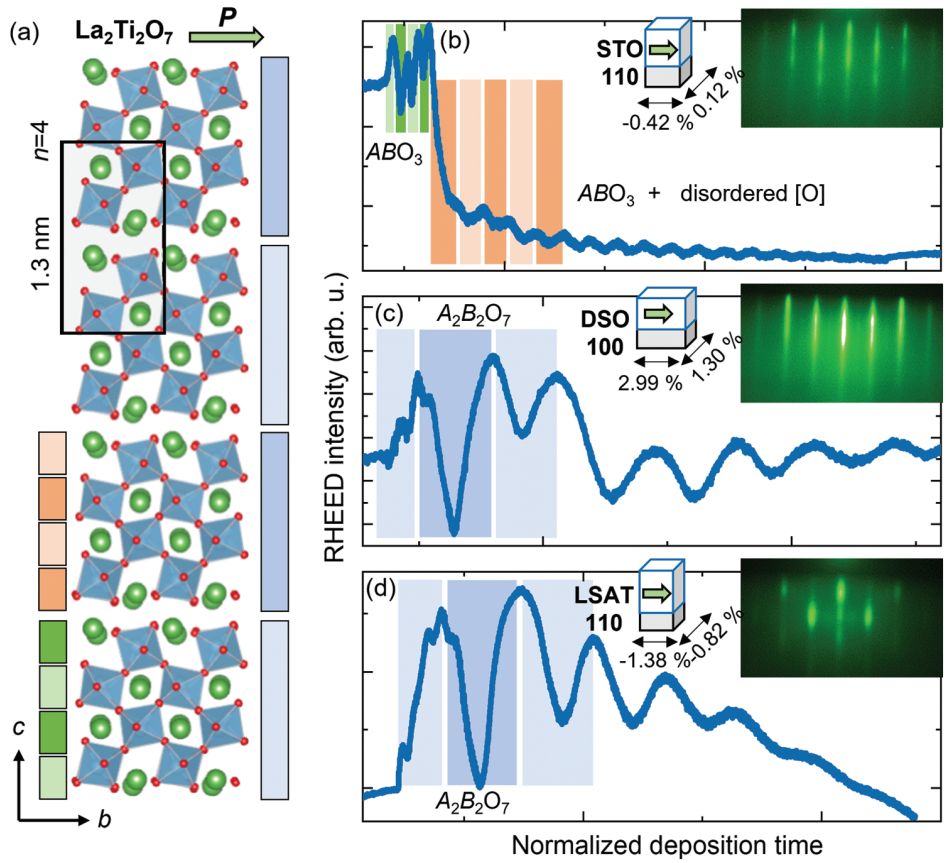

Figure 1. RHEED monitoring of epitaxial LTO film growth. Schematic of the LTO crystal structure viewed along the *b*-*c* plane, showing uniaxial polarization along the *b*-axis. The black rectangular box represents one unit cell, which has a height of 1.3 nm along the out-of-plane *c*-axis. b–d) RHEED intensity traces for LTO films grown on three substrates at 800 °C, partial oxygen pressure of $6 \cdot 10^{-2}$ mbar, laser repetition rate of 1 Hz with fluence of 1.2 J cm^{-2}: b) STO (110) with negligible strain, c) DSO (100) with tensile strain, and d) LSAT (110) with compressive strain. Insets display the corresponding epitaxial strain orientations along the in-plane axes and the observed RHEED patterns for each substrate.

full-layer coverage. Lastly, we repeat the same deposition of the LTO film on the LSAT (110) substrate, inducing compressive in-plane strain. Similarly to the deposition on DSO, we record pronounced coalescent layer-by-layer oscillations with a similar period corresponding to the deposition of one full LTO unit cell (marked in blue), see Figure 1d. However, the rapidly decreasing RHEED intensity and fading oscillations suggest that this growth mode is sustainable only up to six unit cells under this strain state, eventually transitioning to a 3D island growth as captured in the RHEED pattern (inset of Figure 1d).

2.2. Tensile Strain as a Way to Stabilize CG Phase Amid Competing Phases in LTO Films

To shed light on the marked differences in the LTO growth dynamics on the three different substrates, we employ atomic force microscopy (AFM) to evaluate the resulting surface morphology, PFM to measure their local ferroelectric response, and XRD to investigate their macroscopic crystallinity. The films on STO are atomically flat (see **Figure** 2a), which is consistent with the layering of perovskite units. The lateral PFM (LPFM) measurements (see Figure 2b), however, show no signal indicative of ferroelectric polarization or the existence of ferroelectric domains. This result is further corroborated by XRD showing no 001-oriented peaks corresponding to the CG phase (the theoretical[30] position of the most intense LTO 004 reflection is indicated with a dashed line). The peaks are shifted to lower 2Θ values and can instead be associated with the reflections of orthorhombic, kinetically-favored metastable γ polymorph[31,36] (see Figure 2c). This suggests that while the coverage with perovskite-like planes was taking place in a controlled layer-by-layer fashion, the oxygen planes were not provided enough energy to crystallize in an ordered manner, i.e., every four perovskite layers, see schematic in Figure 2d. This observation goes hand in hand with the work of Havella et al.,[31] which described the competition between the more thermodynamically stable CG phase and the kinetically favored metastable γ polymorph. We find that to achieve a layered $A_2B_2O_7$ phase on STO (110) without oxygen plane disorder, the films must be deposited at very high substrate temperatures (above 1000 °C). However, at these temperatures, the adsorbed species gain excess kinetic energy, resulting in a step-flow growth mode. This mode produces no RHEED oscillations, limiting the ability to monitor film thickness with unit-cell precision. Additionally, the high kinetic energy, combined with the splashing of ejected target particles, leads to rougher surfaces,

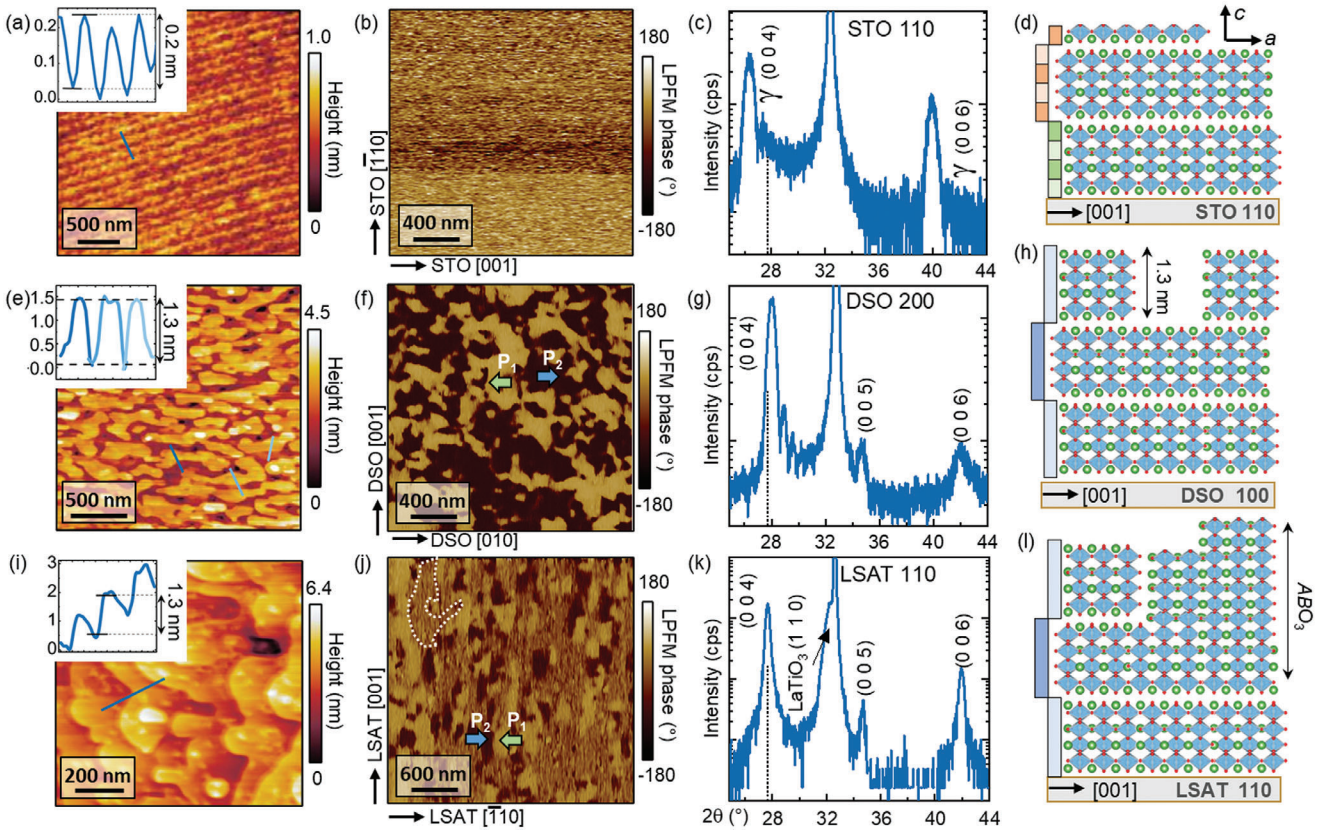

Figure 2. Elucidating LTO growth modes on STO, DSO, and LSAT substrates through structural and ferroelectric analysis. a–d) For LTO films on STO (110): a) AFM image showing atomically flat surface, b) PFM image indicating lack of ferroelectric polarization, c) XRD diffractogram showing the presence of a metastable γ phase, and d) schematic of the corresponding growth mode. e–h) On DSO (100): e) AFM image displaying islands of 1.3 nm in height, f) PFM image revealing in-plane-polarized ferroelectric domains, g) XRD pattern showing 00*l*-oriented CG phase and Laue fringes indicative of high-quality film, and h) growth schematic illustrating coalescent layer-by-layer mode. i–l) On LSAT (110): i) AFM image of flat step terraces with a height of 1.3 nm, j) PFM image with three contrast levels suggesting mixed-phase regions, k) XRD diffractogram identifying the CG and perovskite phases, and l) corresponding growth schematic.

further complicating film quality control, see Note S2 (Supporting Information).

The post-deposition AFM measurements of films grown on DSO (Figure 2e) reveal precisely 1.3-nm-high islands on atomically flat surfaces, confirming the coalescence of complete $A_2B_2O_7$ unit cells. The LPFM measurement (Figure 2f) shows well-defined nanoscale domains with two polarization directions along the *b* polar axis, indicating that the tensile-strained film is stabilized in the ferroelectric phase (see Note S3, Supporting Information for vector PFM analysis). Additionally, the XRD diffractogram in Figure 2g confirms the pure 001-oriented CG phase, free of any parasitic phases, with Laue thickness fringes around the 004 reflection, highlighting high film quality and sharp interfaces. The coalescent layer-by-layer growth mode, illustrated in Figure 2h, accounts for the high crystallinity of the Carpy-Galy LTO films on DSO. This mode, where unit cells initially grow as isolated islands that later merge into flat layers, mirrors growth behavior observed in Aurivillius phase films.[9,10] Remarkably, this growth mode is sustained on DSO even at high substrate temperatures, achieving optimal crystallinity at 1075 °C, unlike on the lattice-matched STO substrate, where elevated temperatures favor a step-flow growth mode.

At first glance, atomically flat step terraces of 1.3 nm in height (shown in Figure 2i) suggest the successful stabilization of the CG LTO phase on LSAT substrates. Nevertheless, the PFM measurements reveal three contrast levels (Figure 2j): while the brighter and darker areas correspond to the two in-plane-polarized domain variants previously observed for the LTO domains on DSO (cf. Figure 2f), the intermediate signal suggests that those areas (e.g., the one outlined with a dashed line) are not ferroelectric. This is further supported by XRD results (Figure 2k), which show not only the CG 00*l* reflections but also a significant presence of the 110-oriented non-polar $LaTiO_3$ perovskite phase in the pristine films. All this gives insights into the LTO growth mode on LSAT (schematized in Figure 2l): deposition begins with a coalescent layer-by-layer growth mode, but as thickness increases, $LaTiO_3$ perovskite units begin to incorporate, leading to a suppression of RHEED oscillations and the emergence of 3D growth patterns in RHEED (see Figure 1d). On LSAT this growth behavior is consistent across deposition temperatures ranging from 800 to 1100 °C.

Together, these results from Figures 1 and 2 indicate that a finite amount of epitaxial strain, either tensile or compressive, is crucial for stabilizing the layer-by-layer growth mode, where the

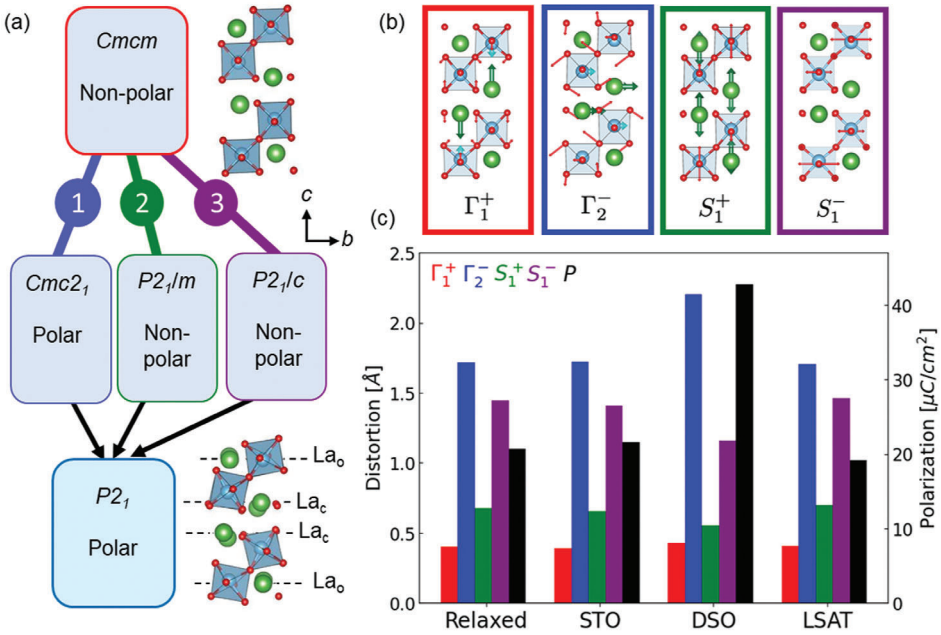

Figure 3. Distortion modes in LTO and their dependence on epitaxial strain. a) Schematic of potential phase transitions from high-symmetry non-polar parent phase *Cmcm* to ferroelectric phase $P2_1$ through pathways 1–3. In the polar $P2_1$ unit cell, we can identify two La positions: the central La ions closest to the oxygen spacer (La_c) and outer La ions (La_o). b) Illustration of distortion modes connecting *Cmcm* and $P2_1$ space groups. c) Comparison of distortion amplitudes across different substrates indicating resilience to epitaxial strain with most pronounced changes in the amplitudes of S_1^+, S_1^-, and polar Γ_2^- modes. Black bars correspond to the resulting polarization values calculated with DFT, see Note S5 (Supporting Information).

full $A_2B_2O_7$ layers coalesce into atomically flat layers. This behavior is highly unusual when compared to traditional perovskite ferroelectrics, which typically achieve optimal crystallinity with minimal lattice mismatch. Notably, the CG phase is most effectively stabilized on DSO substrates that exert a 2.99% tensile strain along the polar *b*-axis. Such significant strain is rarely accommodated well in epitaxial films; however, in this case, it not only supports growth but also enhances the proper layering of the CG phase. This observation suggests that the role of epitaxial strain is not merely to stabilize the CG phase itself, but rather to destabilize competing phases such as the (110)-oriented perovskite and the kinetically favored metastable polymorphs, thereby enabling the selective stabilization of the layered CG structure. This approach could potentially serve as a universal strategy for stabilizing other members of the CG family.

2.3. Sequential Phase Transitions, Symmetry-Adapted Distortions and their Interplay with Epitaxial Strain

Given the strong interplay between strain and polar displacements in ferroelectrics, we turn to DFT calculations to gain deeper insight into the strain-dependent stability of the CG phase observed experimentally. Specifically, we explore how symmetry-adapted distortions within the LTO unit cell respond to varying epitaxial strain. The space group of the high-symmetry phase at > 1500 °C[29] is *Cmcm*,[23,24,29] and its calculated phonon band structure reveals various structural instabilities that relate the structure to lower symmetry phases (Note S4, Supporting Information). The low-temperature ferroelectric phase of LTO is widely accepted as $P2_1$, which is supported by its phonon spectrum, showing no remaining instabilities (Note S4, Supporting Information). Nevertheless, the transition pathway between them remains debated,[23,37,38] see **Figure 3a**. The group-subgroup relationship between *Cmcm* and $P2_1$ suggests two sequential phase transitions, and by performing a symmetry analysis we find four symmetry-adapted distortions connecting them. The first mode is the ferroelectric mode, Γ_2^-, which consists of a rotation of the octahedra along the *c* axis and at the same time a lateral movement of central lanthanum (La_c) ions, leading to a non-zero dipole moment along the *b*-axis. This mechanism of inducing polarization was dubbed topological ferroelectricity.[24] Additionally, we identify two unit-cell doubling distortions, S_1^+ (octahedral tilts along *b* and anti-polar La shifts) and S_1^- (octahedral tilts along *c*), see Figure 3b. These three symmetry-breaking distortions couple to the non-symmetry-breaking Γ_1^+ mode, which contains anti-polar shifts of La_c atoms and minor TiO_6 distortions.

This combination of distortions suggests three possible phase transition pathways. Two of these, *Cmcm* → $Cmc2_1$ → $P2_1$[24] and *Cmcm* → $P2_1/m$ → $P2_1$[23] have been previously discussed in the literature and are labeled as paths 1 and 2 in Figure 3a. We propose a third, previously unexplored sequence, *Cmcm* → $P2_1/c$ → $P2_1$, labeled as path 3, in which the S_1^- distortion mediates the intermediate phase. Our calculations reveal that the primary distortions are the S_1^- tilts and the polar Γ_2^- displacements (see Figure 3c), together contributing ca. 75% of the total displacements. This suggests that these two modes likely act as primary order parameters in the phase transition, favoring either pathway 1 or 3. While some experimental evidence indicates $Cmc2_1$ as the intermediate phase,[37] the instability of the S_1^- phonon, along

with its flat phonon band (see Note S4, Supporting Information), suggests that pathway 3 may be linked to experimentally observed incommensurate intermediate phases.[38] Ultimately, the exact sequence may depend on synthesis conditions, as was observed for $LaTaO_4$,[39] the $n = 2$ member of the CG series.

After identifying the main irreducible representations in the ferroelectric phase, we examined their response to the epitaxial strain imposed by each of the substrates. Across the three substrates studied, we found that the distortions are generally resilient to considerable strain values (see Figure 3c). STO, which provides the closest epitaxial match, shows distortion amplitudes nearly identical to those in the relaxed structure. Similarly, LSAT, which introduces about 1% compressive strain along *a* and *b*, produces only minor changes in distortion amplitude. This resilience is unusual but aligns with LTO's high ferroelectric T_c, underscoring the material's robust ferroelectric state. The effect is notably different on DSO, which imposes a substantial tensile strain of almost 3% along the *b* direction and 1% along *a*. While the overall distortion amplitude on DSO is only moderately increased relative to relaxed LTO, a significant redistribution among the distortion modes occurs: the polar Γ_2^- mode rises by approximately 30%, while S_1^+ and S_1^- tilt patterns decrease slightly. These observations suggest that tensile strain in LTO significantly enhances its in-plane polarization.

Motivated by this finding, we calculate the spontaneous polarization for the different strain states (see Figure 3c and Note S5, Supporting Information), and find spontaneous polarization of 20.7 μCcm^{-2} for the relaxed structure, comparable to the literature value.[23] Under epitaxial strain, we obtain 21.6 and 19.2 μCcm^{-2} for STO and LSAT respectively. The most striking result is observed with DSO, where the polarization value doubles to 42.7 μCcm^{-2}. Note S5 (Supporting Information) further quantifies the polarization with the effective strain along the different axes for each substrate, highlighting a non-linear increase of the spontaneous polarization as a function of strain, particularly on DSO substrates.

2.4. Achieving CG Phase Stabilization Across Substrates via Post-Annealing: Structural Characterization and Mapping of Atomic Displacements

While the tensile strain of the DSO substrate is required to stabilize the CG phase during the deposition through the controlled layer-by-layer growth mode, literature reports indicate that annealing LTO films in an oxygen atmosphere at temperatures above 1100 °C can serve as a post-deposition method for obtaining the CG phase.[35,40–42] This strategy indeed proved to be effective for rectifying the correct CG layering on the STO and LSAT substrates, which fail to stabilize it in the pristine films. We stress here, however, that such thermal intervention comes at the expense of losing detailed control over structural properties such as surface morphology and exact RHEED-monitored thickness. **Figure** 4a displays the diffractograms of the post-annealed LTO films on STO and LSAT substrates alongside the pristine LTO film on DSO: all three films now exhibit the 001-oriented CG phase, free from detectable impurities (see Note S6, Supporting Information) and crystal twinning. Reciprocal space mapping of LTO (0 2 9) and (0 -2 9) reflections shown in Figure 4b reveals that the films are coherently strained to the STO substrate, while strain relaxation is observed on both DSO and LSAT. Despite not being fully strained to their substrates, these films retain characteristics of the tensile and compressive strains applied. For example, shifts in the 004 reflections relative to the bulk out-of-plane lattice parameter[30] (marked with a dashed line, corresponding to $d_\perp = 1.2864$ nm) are evident in Figure 4a, where the LTO out-of-plane lattice parameter is elongated by 0.2% on LSAT and shortened by -0.3% and -1.0% on STO and DSO, respectively, consistent with the expected strain effects.

To complement the macroscopic structural analysis, we conducted atomically-resolved high-angle annular dark-field scanning transmission electron microscopy (HAADF-STEM) imaging of the LTO films on STO (110). The image displayed in Figure 4c shows the characteristic layering of atomic planes of the CG phase in the *b*–*c* plane of the film. La ions have the brightest contrast and form characteristic zig-zag-like slabs: with and without teardrop shape distortions in La, that alternate every two atomic rows along the out-of-plane $[001]_{LTO}$ direction. The distortions, seen in La ions closest to the oxygen spacers (marked La_c in Figure 3a), arise from the Γ_2^- polar distortion mode (shown in Figure 3b), which induces lateral movement of La ions along the *b*-axis. In combination with the anti-polar (Γ_1^+ and $S1^+$) movement along the *c* axis, this leads to the appearance of the teardrop-like La doublets. In contrast, the two outer La ions, positioned further from the oxygen planes (marked La_o in Figure 3a), exhibit no in-plane displacement and therefore appear perfectly spherical and one can only observe the lateral movement of Ti atoms positioned above and below them, again consistent with the Γ_2^- mode. The inset in the top right provides the overlay with the theoretical atomic positions, bonds, and oxygen octahedra associated with the monoclinic space group $P2_1$.[30] A selected portion of the film (red box) is analyzed with 4D-STEM to identify the exact positions of La, oxygen (O), and titanium (Ti) ions (Figure 4d).

2.5. Significantly Enhanced Ferroelectricity with No Critical Thickness, Ferroelectric Domains and Their Formation Mechanisms in Post-Annealed LTO Films

After confirming the structural quality of our LTO films on all three substrates, we proceeded to further characterization of their ferroelectric properties. **Figure** 5a illustrates the ferroelectric switching characteristics of a representative 56-nm-thick LTO film on STO (110) measured using a Positive Up Negative Down (PUND) pulse scheme. The field is applied in the plane of the film along the polar axis $[0\ 1\ 0]_{LTO}$. We obtain a clear ferroelectric polarization hysteresis loop in line with the expected uniaxial polar anisotropy observed in vector PFM measurements (current-voltage characteristics and additional details are outlined in Note S7, Supporting Information). The measured polarization of 18.3 μCcm^{-2} is nearly four times higher than 5 μCcm^{-2} reported for bulk LTO crystals[29] or 2.8 μCcm^{-2} measured for LTO films on Nb-doped STO (110),[43] but not too far off from 21 μCcm^{-2} predicted from DFT calculations (see Section 2.3). Yet, it remains unclear whether this enhancement stems mainly from epitaxial strain or from the overall improved crystal quality of our films. A promising route to disentangle these contributions would be to release LTO layers as freestanding membranes using a sacrificial

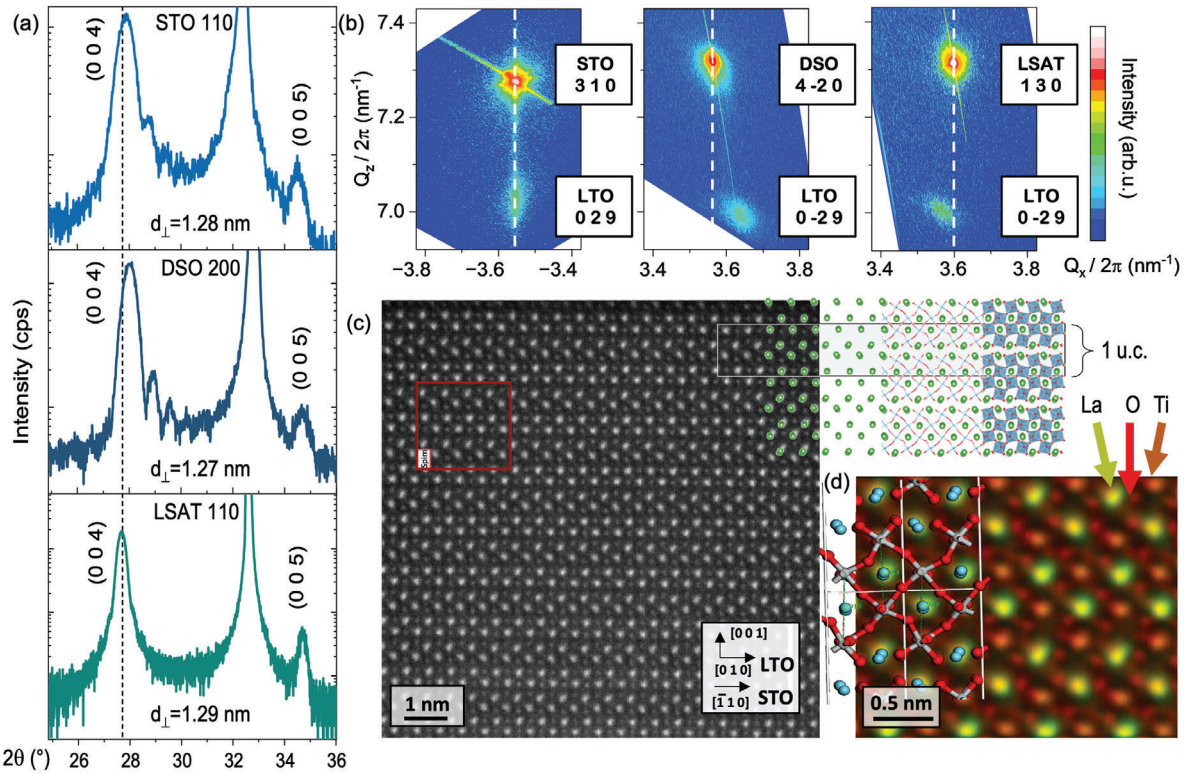

Figure 4. Structural properties of LTO films of the CG phase: post-annealed on STO and LSAT and as-grown on DSO. a) Diffractograms of LTO films show the stabilized 001-oriented CG phase. Strain effects are evident from the shifts of the 004 reflections around the literature value (dashed line). b) Reciprocal space maps of LTO (0 2 9) and (0 -2 9) reflections reveal coherently strained films on the STO substrate, with relaxation observed on DSO and LSAT. c) HAADF-STEM image of the LTO film on STO (110) displays the precise atomic layering in the *b-c* plane, highlighting the alternation of La ions' zig-zag rows, indicative of polar distortions. The inset in the top right provides the overlay with the theoretical atomic positions, bonds, and oxygen octahedra. d) 4D-STEM analysis (area marked with a red box in c)) with superimposed theoretical atomic positions of La, Ti, and O atoms.

$Sr_3Al_2O_6$ buffer on STO (110).[44] Freed from the substrate constraints, such membranes[45] would relax interfacial and stacking defects while retaining epitaxial order, thus allowing a clearer assessment of the intrinsic ferroelectric response in our CG films.

Compared to other classes of ferroelectric materials, the polarization measured in our LTO films exceeds typical values observed in van der Waals ferroelectrics[46] and is slightly below those reported for binary and perovskite oxides, such as 34 μCcm^{-2} in $Hf_{0.5}Zr_{0.5}O_2$[47] and 30 μCcm^{-2} in $BaTiO_3$.[48] Notably, the single-unit-cell (1.3 nm) thickness limit for ferroelectricity in LTO films is comparable to that of hafnium-based binary oxides[49] and significantly thinner than what is typically observed in traditional perovskite-based ferroelectrics.[50–53] The combination of high polarization and exceptional thickness scalability establishes LTO as a competitive material in the realm of nanoscale ferroelectrics, with a detailed property comparison provided in Note S7 and Table S2 (Supporting Information).

The substantial enhancement observed in LTO polarization emphasizes the importance of epitaxy for improved crystal quality. Furthermore, the coercive field of 16.9 kVcm^{-1} is more than three times lower than the previously reported value,[19] rendering such LTO films on STO even more attractive for device applications as their operational voltage could be significantly reduced. However, we observe a significant increase in the coercive field, when LTO films are thinner (see Note S8, Supporting Information) or are deposited on LSAT and DSO substrates (see Note S7, Supporting Information), which is likely due to the crystal defects pinning polarization[54] at the interface with the substrate as well as within the film volume, as LTO is not fully strained on neither LSAT nor DSO substrates (refer to Figure 4b).

Building on the insights gained from the macroscopic polarization analysis, we now turn our attention to the PFM-based ferroelectric domain analysis. While there have been reports on the PFM measurements performed on the LTO films in the literature, they were obscured by significant surface roughness creating a non-negligible cross-talk between topography and piezoresponse-related tip torsion and buckling. In our case, the achievement of atomically flat films with uniaxial in-plane polarization along their *b*-axis (refer to Note S3, Supporting Information) facilitates the clear identification of ferroelectric domains in CG films. Figure 5b displays LPFM phase images of ferroelectric in-plane domains recorded for ca. 20-unit-cell-thick LTO films on the three different substrates. Across all three strain states, the patterns contain the two domain variants with polarization pointing along $[0\ 1\ 0]_{LTO}$ and $[0\ \bar{1}\ 0]_{LTO}$. We noted two general trends for domain scaling: ferroelectric domain size increases with both film thickness and compressive strain.

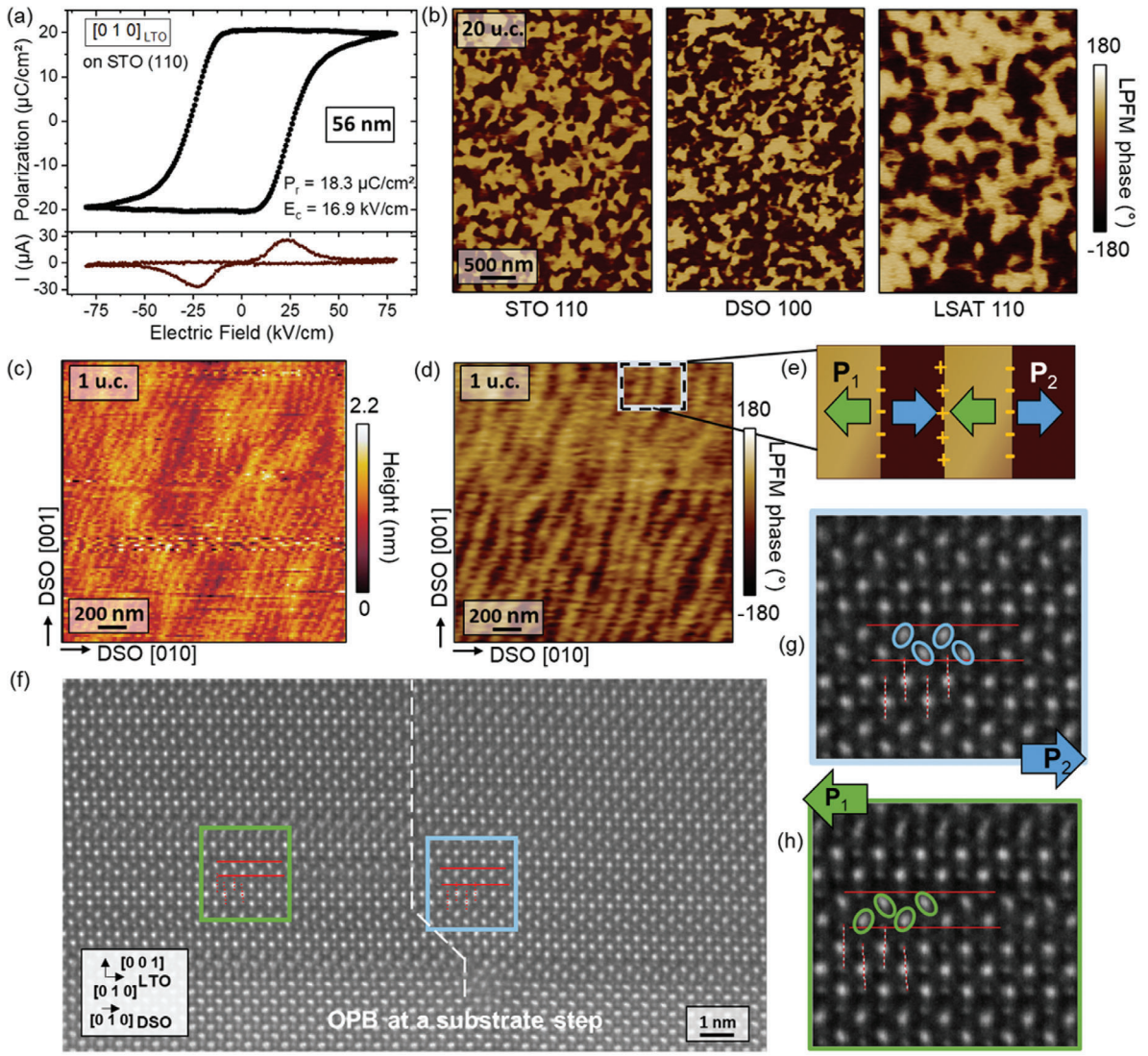

Figure 5. Ferroelectric properties of the LTO films. a) Polarization-Electric Field (P-E) hysteresis loops and switching current recorded for a 56-nm-thick LTO film on STO (110), displaying clear ferroelectric behavior along the polar axis $[0\ 1\ 0]_{LTO}$. b) LPFM phase images showing in-plane ferroelectric domains in ca. 20-unit-cell (u.c.)-thick LTO films on STO, DSO, and LSAT. The images reveal two domain variants with polarizations along $[0\ 1\ 0]_{LTO}$ and $[0\ \bar{1}\ 0]_{LTO}$. c) Topography of a monolayer LTO film on DSO with atomically flat terraces. d) The corresponding PFM image shows in-plane-polarized stripe domains, confirming the ferroelectric functionality of just a 1.3-nm-thick LTO layer. e) Schematic of the stripe domain pattern giving rise to nominally charged domain walls with alternating accumulations of mobile screening charges. f) HAADF-STEM imaging of the LTO film adjacent to a DSO substrate step reveals an out-of-phase boundary (OPB) in the film. Atomically resolved displacements g) to the right and h) to the left of the OPB show opposite in-plane polarization directions. This suggests the presence of a tail-to-tail domain wall pinned at the substrate step position.

In-plane-polarized ferroelectric films should, in principle, exhibit no critical thickness for ferroelectricity. This is because in-plane polarization has no bound charges localized on the film surfaces, thereby avoiding the depolarizing fields that usually destabilize ferroelectricity at reduced thicknesses. The stabilized layer-by-layer growth mode of LTO films on DSO gives us the means to prepare ultrathin films of just 1 unit cell.c. in thickness and test this. Figure 5c displays AFM topography of a 1-unit-cell-thick LTO coverage, maintaining atomic step terraces of the underlying DSO substrate. The corresponding LPFM image (Figure 5d) reveals well-ordered stripe domains extending over hundreds of microns, confirming that a mere 1.3-nm-thick layer of LTO already exhibits its ferroelectric functionality. As the polarization is along the *b*-axis, such a domain pattern can be described as a network of partially charged domain walls with alternating accumulations of screening mobile charges, as schematized in Figure 5e. The similarity between the domain shape and the atomic terraces in the topography (cf. Figure 5c) suggests that structural defects at each substrate step likely trigger the reversal of in-plane polarization from one domain to the next. This hypothesis is supported by HAADF-STEM imaging of the LTO film near a DSO substrate step (Figure 5f), where the substrate step induces an out-of-register shift between the LTO unit cells, known as an

out-of-phase boundary (OPB).[55] Analysis of the atomic displacements in the film to the right of the OPB (marked by a blue box and zoomed in in Figure 5g) shows that the teardrop-like La displacements point left, while the non-distorted La columns are displaced right relative to the Ti-Ti line, indicating rightward polarization. Conversely, to the left of the OPB (marked by a green box and zoomed in Figure 5h), the direction of the teardrop displacements reverses, pointing right, while the non-distorted La columns shift left, confirming the inversion of polarization direction and the formation of a tail-to-tail domain wall at the OPB. This domain-formation mechanism, similar to that observed in layered in-plane-polarized Aurivillius systems,[12,56] arises from discontinuities in electrostatic boundary conditions due to structural defects. It is likely universally applicable across all layered compounds, such as Ruddlesden-Popper or Dion-Jacobson phases, when they are epitaxially stabilized as uniaxial in-plane ferroelectrics.

3. Conclusion

In this work, we systematically investigated the epitaxial growth of LTO films and the influence of various strain states on the stability of the layered CG phase. We demonstrate that high-quality films exhibit robust ferroelectric polarization around 18 μCcm^{-2} – more than three times higher than previously reported, aligning with theoretical predictions. Our study reveals a remarkable resilience of the ferroelectric phase under epitaxial strain. Specifically, a tensile strain of 3% along the polar axis, introduced by DSO (100) substrates, not only preserves but enhances the CG phase, promoting a coalescent layer-by-layer growth mode. In contrast, STO (110) and LSAT (110) substrates, exerting negligible or compressive strain, initially fail to stabilize the CG phase but can achieve phase stabilization through post-deposition annealing. Complementing experimental findings, our DFT calculations show that the CG phase maintains structural stability under varying strains, even predicting a doubling of polarization on DSO substrates. Lastly, we demonstrate that ferroelectricity is retained down to a single unit cell, with stripe-domain patterns indicating a complex interplay between substrate imperfections and domain configurations. These findings establish Carpy-Galy thin films as a promising platform for exploring ultrathin ferroelectric applications. Our work invites further research into novel functionalities in this layered family, which could expand the capabilities of next-generation electronic devices.

4. Experimental Section

Thin-Film Growth: $La_2Ti_2O_7$ (LTO) films were grown on $SrTiO_3$ (STO) (110) (Surfacenet GmbH), $DyScO_3$ (DSO) (100) (Surfacenet GmbH), and $LaAlO_3$-Sr_2TaAlO_6 (LSAT) (110) substrates (CrysTec GmbH). The STO substrates underwent chemical treatment with a buffered HF solution, and all substrates were thermally treated to form well-defined atomic step terraces.[57] The films were deposited using a single stoichiometric $La_2Ti_2O_7$ target by pulsed laser deposition using a 248 nm KrF excimer laser, at substrate temperatures of 800 to 1100 °C, oxygen partial pressure of $5{\cdot}10^{-3}$ to $6{\cdot}10^{-2}$ mbar, laser fluence of 1.0 to 1.4 J cm^{-2} with a laser spot size of 3.5 ± 0.3 mm^2 and 1 Hz repetition rate.

Optimized parameters for each substrate were as follows: on STO (110): 800 °C, $6{\cdot}10^{-2}$ mbar, 1.2 J cm^{-2}, followed by post-annealing in an oxygen atmosphere at 1100 °C for 3 h; on DSO (100): 1075 °C, $7.5{\cdot}10^{-3}$ mbar, 1.4 J cm^{-2}, with no post-annealing required; on LSAT (110): 1075 °C, $5{\cdot}10^{-3}$ mbar, 1.2 J cm^{-2}, followed by post-annealing in an oxygen atmosphere at 1100 °C for 3 h. The thickness of the films was continuously monitored using RHEED during growth and verified post-deposition by X-ray reflectivity.

X-ray Diffraction: The crystalline structure of thin films was analyzed by X-ray diffraction, X-ray reflectivity, and reciprocal space mapping measurements using a four-circle X-ray diffractometer (Panalytical Empyrean and Rigaku SmartLab).

Scanning Probe Microscopy: Atomic and piezoresponse force microscopy acquisition was performed in contact mode in a Nanoscope V multimode (Bruker) microscope with two external SR830 lock-in amplifiers (Stanford Research) for simultaneous acquisition of in-plane and out-of-plane piezoresponse. The data acquisition was performed using AC modulation of 5–12 V (peak-to-peak) at 35 kHz applied to the Pt-coated tip (2.7 Nm^{-1} cantilever, ElectriAll-In-One). Images of in-plane-polarized domains were recorded through cantilever torsion mode when measuring with a cantilever perpendicular to the uniaxial LTO polarization axis $[0\ 1\ 0]_{LTO}$.

Interdigitated Electrode Design: The interdigitated electrodes were patterned using maskless projection photolithography on a Smart Print UV system (microlight3D) and electron beam lithography (Raith Pioneer Two). This was followed by the sputtering of a 3 nm titanium (Ti) adhesion layer and a 10 to 20 nm gold (Au) layer or a 10 to 20 nm platinum (Pt) layer. The patterning process was completed with a lift-off process. Electrode patterns comprising up to 200 fingers were used. For films with low coercive fields, devices were used with a finger and gap width of 5 μm each, and a length of 995 μm (fabricated with projection lithography). For films with higher coercive fields, to enable the application of higher electric fields, devices were used with a finger and gap width of 1 μm each, and a finger length of 248 μm (fabricated with electron beam lithography). See Note S7 (Supporting Information) for details on the device design.

Macroscopic Ferroelectric Polarization Switching: Ferroelectric properties of the LTO films were characterized with a ferroelectric tester (Radiant Technologies). The *P–E* loops were measured using the positive-up negative-down (PUND) method. This technique involved applying a sequence of five electrical pulses, each with a frequency ranging from 0.1 to 10 kHz. This allowed for precise evaluation of the intrinsic switching properties of the ferroelectric films, free from extrinsic contributions such as leakage current. See Note S9 (Supporting Information) for details on the optimization of switching parameters.

Scanning Transmission Electron Microscopy (STEM): STEM experiments were performed using a Cs-corrected Nion USTEM operated at 200 keV, with a probe current of approximately 20 pA and a probe size of about 80 pm. HAADF images were obtained with typical 80–200 mrad collection angles. 4D-STEM images were also obtained by collecting the entire diffraction patterns, with a typical spatial step of 10 to 20 pm. Images were then generated (e.g., Figure 4d) by computing the divergence of the center-of-mass of the diffraction patterns, which roughly approximate charge distribution images. Samples were prepared for STEM using a focused ion beam, with a Ga beam at 30, 16, and 8 keV, followed by final surface cleaning at 5 and 2 keV.

Density Functional Theory (DFT) Calculations: DFT calculations were performed using the VASP[58,59] code. A converged 6 × 6 × 2 grid was used for the 44 atom $P2_1$ unit cell and 6 × 6 × 6 for the 22 atom *Cmcm* cell. A planewave cutoff of 500 eV was employed. We used the PBEsol functional and[61] pseudopotentials with the following electrons in the valence: for La: $5s^2 5p^6 6s^2 5d^1$; for Ti: $4s^2 3d^2$; and for O: $2s^2 2p^4$. In order to calculate the adjustment of the material to the substrate, the *a* and *b* lattice parameters are fixed, and the relaxation of the out-of-plane lattice parameter and the monoclinic angle between the *a* and *c* axes is allowed. Internal forces were relaxed down to a maximal force of 0.01 eVÅ^{-1}. Symmetry mode analysis comparing *Cmcm* and $P2_1$ was performed using the AMPLIMODES sofware.[60]

Acknowledgements

E.G. acknowledges the Swiss National Science Foundation for financial support under Project No. P500PT_214449. M.B. and A.S.G. acknowledge ERC for funding under PoC UPLIFT Project No. 101113273. The authors thank Luis Moreno Vicente-Arche for experimental support. [Correction added on February 18, 2025, after first online publication: Figure 2 has been updated.]

Author Contributions

The thin-film growth, scanning probe microscopy, and XRD structural analysis were conducted by E.G. Interdigitated top electrodes were designed and patterned by A.S.G. with E.G. Ferroelectric switching experiments were performed by E.G. and A.S.G. X.L. and A.G. carried out the STEM investigations. L.I. supported the thin-film growth and XRD experiments. DFT calculations were performed by Q.N.M. The experiment was designed by E.G. with M.B., who also supervised the study. All authors contributed to the discussion of the results. E.G. wrote the manuscript with the inputs from all authors.

[1] J. Junquera, P. Ghosez, *Nature* **2003**, *422*, 506.
[2] M. Li, H. Tan, W. Duan, *Phys. Chem. Chem. Phys.* **2020**, *22*, 14415.
[3] E. Bousquet, M. Dawber, N. Stucki, C. Lichtensteiger, P. Hermet, S. Gariglio, J. M. Triscone, P. Ghosez, *Nature* **2008**, *452*, 732.
[4] M. H. Park, Y. H. Lee, T. Mikolajick, U. Schroeder, C. S. Hwang, *MRS Commun.* **2018**, *8*, 795.
[5] Z. Guan, H. Hu, X. Shen, P. Xiang, N. Zhong, J. Chu, C. Duan, *Adv. Electron. Mater.* **2020**, *6*, 1900818.
[6] W. J. Xu, S. Kopyl, A. Kholkin, J. Rocha, *Coord. Chem. Rev.* **2019**, *387*, 398.
[7] N. A. Benedek, J. M. Rondinelli, H. Djani, P. Ghosez, P. Lightfoot, *Dalton Trans.* **2015**, *44*, 10543.
[8] L. Keeney, Z. Saghi, M. O'Sullivan, J. Alaria, M. Schmidt, L. Colfer, *Chem. Mater.* **2020**, *32*, 10511.
[9] E. Gradauskaite, M. Campanini, B. Biswas, C. W. Schneider, M. Fiebig, M. D. Rossell, M. Trassin, *Adv. Mater. Interfaces* **2020**, *7*, 2000202.
[10] E. Gradauskaite, N. Gray, M. Campanini, M. D. Rossell, M. Trassin, *Chem. Mater.* **2021**, *33*, 9439.
[11] L. Keeney, R. J. Smith, M. Palizdar, M. Schmidt, A. J. Bell, J. N. Coleman, R. W. Whatmore, *Adv. Electron. Mater.* **2020**, *6*, 1901264.
[12] E. Gradauskaite, K. A. Hunnestad, Q. N. Meier, D. Meier, M. Trassin, *Chem. Mater.* **2022**, *34*, 6468.
[13] K. Moore, E. N. O'Connell, S. M. Griffin, C. Downing, L. Colfer, M. Schmidt, V. Nicolosi, U. Bangert, L. Keeney, M. Conroy, *ACS Appl. Mater. Interfaces* **2022**, *14*, 5525.
[14] E. Gradauskaite, Q. N. Meier, N. Gray, M. F. Sarott, T. Scharsach, M. Campanini, T. Moran, A. Vogel, K. Del Cid-Ledezma, B. D. Huey, M. D. Rossell, M. Fiebig, M. Trassin, *Nat. Mater.* **2023**, *22*, 1492.
[15] J. G. Bednorz, K. A. Mueller, *Zeitschrift fur Physik B Condens. Matter* **1986**, *64*, 189.
[16] Y. Maeno, H. Hashimoto, K. Yoshida, S. Nishizaki, T. Fujita, J. G. Bednorz, F. Lichtenberg, *Nature* **1994**, *372*, 532.
[17] C. A-Paz de Araujo, J. D. Cuchiaro, L. D. McMillian, M. C. Scott, J. F. Scott, *Nature* **1995**, *374*, 627.
[18] A. Carpy, J. Galy, *Bull. Soc. Fr. Ceram.* **1974**, *97*, 484.
[19] S. Nanamatsu, M. Kimura, T. Kawamura, *J. Phys. Soc. Jpn.* **1975**, *38*, 817.
[20] V. A. Isupov, *Ferroelectrics* **1999**, *220*, 79.
[21] F. Lichtenberg, *Prog. Solid State Chem.* **2001**, *29*, 1.
[22] F. Lichtenberg, A. Herrnberger, K. Wiedenmann, *Prog. Solid State Chem.* **2008**, *36*, 253.
[23] M. Núnez Valdez, N. A. Spaldin, *Polyhedron* **2019**, *171*, 181.
[24] J. López-Pérez, J. Íñiguez, *Phys. Rev. B* **2011**, *84*, 075121.
[25] P. Daniels, R. Tamazyan, C. A. Kuntscher, M. Dressel, F. Lichtenberg, S. Van Smaalen, *Acta Crystallograph. Sect. B Struct. Sci.* **2002**, *58*, 970.
[26] G. W. Howieson, S. Wu, A. S. Gibbs, W. Zhou, J. F. Scott, F. D. Morrison, *Adv. Funct. Mater.* **2020**, *30*, 2004667.
[27] C. Ederer, N. A. Spaldin, *Phys. Rev. B* **2006**, *74*, 020401.
[28] C. A. Kuntscher, S. Schuppler, P. Haas, B. Gorshunov, M. Dressel, M. Grioni, F. Lichtenberg, *Phys. Rev. B - Condens. Matter Mat. Phys.* **2004**, *70*, 1.
[29] S. Nanamatsu, M. Kimura, K. Doi, S. Matsushita, N. Yamada, *Ferroelectrics* **1974**, *8*, 511.
[30] H. W. Schmalle, T. Williams, A. Reller, A. Linden, J. G. Bednorz, *Acta Crystallograph. Sect. B Struct. Sci.* **1993**, *49*, 235.
[31] S. Havelia, S. Wang, K. R. Balasubramaniam, P. A. Salvador, *Cryst. Growth Des.* **2009**, *9*, 4546.
[32] A. Ohtomo, D. A. Muller, J. L. Grazul, H. Y. Hwang, *Appl. Phys. Lett.* **2002**, *80*, 3922.
[33] S. Havelia, K. Balasubramaniam, S. Spurgeon, F. Cormack, P. Salvador, *J. Cryst. Growth* **2008**, *310*, 1985.
[34] S. Havelia, S. Wang, K. Balasubramaniam, P. Salvador, *J. Solid State Chem.* **2009**, *182*, 1603.
[35] T. C. Kaspar, S. Hong, M. E. Bowden, T. Varga, P. Yan, C. Wang, S. R. Spurgeon, R. B. Comes, P. Ramuhalli, C. H. Henager, *Sci. Rep.* **2018**, *8*, 3037.
[36] A. Bayart, S. Saitzek, M.-H. Chambrier, Z. Shao, A. Ferri, M. Huvé, R. Pouhet, A. Tebano, P. Roussel, R. Desfeux, *Cryst. Eng. Comm.* **2013**, *15*, 4341.
[37] N. Ishizawa, F. Marumo, S. Iwai, M. Kimura, T. Kawamura, *Acta Crystallograph. Sect. B: Struct. Crystallogr. Cryst. Chem.* **1982**, *38*, 368.
[38] N. Ishizawa, K. Ninomiya, J. Wang, *Acta Crystallograph. Sect. B Struct. Sci., Cryst. Eng. Mater.* **2019**, *75*, 257.
[39] G. W. Howieson, K. K. Mishra, A. S. Gibbs, R. S. Katiyar, J. F. Scott, F. D. Morrison, M. Carpenter, *Phys. Rev. B* **2021**, *103*, 014119.
[40] Y. Nezu, Y.-Q. Zhang, C. Chen, Y. Ikuhara, H. Ohta, *J. Appl. Phys.* **2017**, *122*, 135305.

[41] T. Yao, Y. Jiang, C. Chen, X. Yan, A. Tao, L. Yang, C. Li, K. Sugo, H. Ohta, H. Ye, Y. Ikuhara, X. Ma, *Nano Lett.* **2020**, *20*, 1047.
[42] B. Qiao, Y. Jiang, T. Yao, A. Tao, X. Yan, C. Gao, X. Li, H. Ohta, C. Chen, X.-L. Ma, H. Ye, *Appl. Surf. Sci.* **2022**, *587*, 151599.
[43] Z. Shao, S. Saitzek, P. Roussel, A. Ferri, E. Bruyer, A. Sayede, M. Rguiti, O. Mentre, R. Desfeux, *Adv. Eng. Mater.* **2011**, *13*, 961.
[44] Z. Lu, J. Liu, J. Feng, X. Zheng, L.-h. Yang, C. Ge, K.-j. Jin, Z. Wang, R.-W. Li, *APL Mater.* **2020**, *8*, 051105.
[45] S. Choo, S. Varshney, H. Liu, S. Sharma, R. D. James, B. Jalan, *Sci. Adv.* **2024**, *10*, eadq8561.
[46] X. Wang, C. Zhu, Y. Deng, R. Duan, J. Chen, Q. Zeng, J. Zhou, Q. Fu, L. You, S. Liu, J. H. Edgar, P. Yu, Z. Liu, *Nat. Commun.* **2021**, *12*, 1109.
[47] Y. Wei, P. Nukala, M. Salverda, S. Matzen, H. J. Zhao, J. Momand, A. S. Everhardt, G. Agnus, G. R. Blake, P. Lecoeur, B. J. Kooi, J. Íñiguez, B. Dkhil, B. Noheda, *Nat. Mater.* **2018**, *17*, 1095.
[48] Y. Jiang, E. Parsonnet, A. Qualls, W. Zhao, S. Susarla, D. Pesquera, A. Dasgupta, M. Acharya, H. Zhang, T. Gosavi, C.-C. Lin, D. E. Nikonov, H. Li, I. A. Young, R. Ramesh, L. W. Martin, *Nat. Mater.* **2022**, *21*, 779.
[49] S. S. Cheema, D. Kwon, N. Shanker, R. Dos Reis, S.-L. Hsu, J. Xiao, H. Zhang, R. Wagner, A. Datar, M. R. McCarter, C. R. Serrao, A. K. Yadav, G. Karbasian, C.-H. Hsu, A. J. Tan, L.-C. Wang, V. Thakare, X. Zhang, A. Mehta, E. Karapetrova, R. V. Chopdekar, P. Shafer, E. Arenholz, C. Hu, R. Proksch, R. Ramesh, J. Ciston, S. Salahuddin, *Nature* **2020**, *580*, 478.
[50] Y. S. Kim, D. H. Kim, J. D. Kim, Y. J. Chang, T. W. Noh, J. H. Kong, K. Char, Y. D. Park, S. D. Bu, J.-G. Yoon, J.-S. Chung, *Appl. Phys. Lett.* **2005**, *86*, 102907.
[51] G. De Luca, N. Strkalj, S. Manz, C. Bouillet, M. Fiebig, M. Trassin, *Nat. Commun.* **2017**, *8*, 1419.
[52] H. Béa, S. Fusil, K. Bouzehouane, M. Bibes, M. Sirena, G. Herranz, E. Jacquet, J. P. Contour, A. Barthélémy, *Jpn. J. Appl. Phys.* **2006**, *45*, L187.
[53] J. J. Steffes, R. A. Ristau, R. Ramesh, B. D. Huey, *Proc. Natl. Acad. Sci. USA* **2019**, *116*, 2413.
[54] S. Saremi, R. Xu, F. I. Allen, J. Maher, J. C. Agar, R. Gao, P. Hosemann, L. W. Martin, *Phys. Rev. Mater.* **2018**, *2*, 1.
[55] M. A. Zurbuchen, W. Tian, X. Q. Pan, D. Fong, S. K. Streiffer, M. E. Hawley, J. Lettieri, Y. Jia, G. Asayama, S. J. Fulk, D. J. Comstock, S. Knapp, A. H. Carim, D. G. Schlom, *J. Mater. Res.* **2007**, *22*, 1439.
[56] L. Keeney, L. Colfer, D. Dutta, M. Schmidt, G. Wei, *Microstructures* **2023**, *3*, 4.
[57] A. Biswas, C.-H. Yang, R. Ramesh, Y. H. Jeong, *Prog. Surf. Sci.* **2017**, *92*, 117.
[58] G. Kresse, J. Hafner, *Physical Review B* **1993**, *47*, 558.
[59] G. Kresse, J. Furthmüller, *Comput. Mater. Sci.* **1996**, *6*, 15.
[60] D. Orobengoa, C. Capillas, M. I. Aroyo, J. M. Perez-Mato, *J. Appl. Crystallogr.* **2009**, *42*, 820.
[61] J. P. Perdew, A. Ruzsinszky, G. I. Csonka, O. A. Vydrov, G. E. Scuseria, L. A. Constantin, X. Zhou, K. Burke, Restoring the Density-Gradient Expansion for Exchange in Solids and Surfaces. Physical Review Letters **2008**, *100*, https://doi.org/10.1103/physrevlett.100.136406.